






Comparison of unit cell coupling for grating-gate and high electron mobility transistor array THz resonant absorbers F

Cite as: J. Appl. Phys. **124**, 093101 (2018); <https://doi.org/10.1063/1.5032102>

Submitted: 02 April 2018 . Accepted: 31 July 2018 . Published Online: 04 September 2018

Hugo O. Condori Quispe , Ashish Chanana , Jimy Encomendero , Mingda Zhu, Nicole Trometer, Ajay Nahata , Debdeep Jena, Huili Grace Xing , and Berardi Sensale-Rodriguez

COLLECTIONS

F This paper was selected as Featured



View Online



Export Citation



CrossMark

ARTICLES YOU MAY BE INTERESTED IN

[Tutorial: Brain-inspired computing using phase-change memory devices](#)

Journal of Applied Physics **124**, 111101 (2018); <https://doi.org/10.1063/1.5042413>

[Breakdown mechanism in 1 kA/cm² and 960 V E-mode \$\beta\$ -Ga₂O₃ vertical transistors](#)

Applied Physics Letters **113**, 122103 (2018); <https://doi.org/10.1063/1.5038105>

[High speed efficient ultraviolet photodetector based on 500nm width multiple WO₃ nanowires](#)

Applied Physics Letters **113**, 101101 (2018); <https://doi.org/10.1063/1.5045249>

Lock-in Amplifiers
Find out more today



 Zurich Instruments



Comparison of unit cell coupling for grating-gate and high electron mobility transistor array THz resonant absorbers

Hugo O. Condori Quispe,¹ Ashish Chanana,¹ Jimmy Encomendero,² Mingda Zhu,² Nicole Trometer,³ Ajay Nahata,¹ Debdeep Jena,² Huili Grace Xing,² and Berardi Sensale-Rodriguez^{1,a)}

¹The University of Utah, Salt Lake City, Utah 84112, USA

²Cornell University, Ithaca, New York 14853, USA

³University of Florida, Gainesville, Florida 32611, USA

(Received 2 April 2018; accepted 31 July 2018; published online 4 September 2018)

We report experimental studies on the excitation of synchronized plasmon resonances in AlGaIn/GaN High Electron Mobility Transistor (HEMT) arrays. In contrast to the commonly employed grating-gate configurations, the analyzed structure contains periodically patterned ohmic contacts to the two-dimensional electron gas, which are laid-out parallel to the gate fingers. In this structure, the terahertz to plasmon coupling mechanism is fundamentally different from that in grating-gate configurations. Whereas the grating-gate configuration constitutes a *coupled* resonant system in which the resonance frequency depends on the grating periodicity, when periodical ohmic contacts are incorporated, the system behaves as a *synchronized* resonant system in which each unit cell is effectively independent. As a result, in a HEMT-array, the resonance is no longer set by the periodicity but rather by the gate and the ungated region length. Experimental results of fabricated samples compare well with numerical simulations and theoretical expectations. Our work demonstrates that the proposed approach allows: (i) more efficient excitation of high order plasmon modes and (ii) superior overall terahertz to plasmon coupling, even in configurations having less number of devices per unit area. From this perspective, our results reveal a simple way to enhance the terahertz to plasmon coupling and thus improve the performance of electron plasma wave-based devices; this effect can be exploited, for example, to improve the response of HEMT-based terahertz detectors. *Published by AIP Publishing.* <https://doi.org/10.1063/1.5032102>

I. INTRODUCTION

The terahertz (THz) frequency range is a region of the electromagnetic spectrum loosely defined between 0.1 and 10 THz, i.e., between the microwave and infra-red (IR) regions of the spectrum. In this spectral region, both electrical and optical phenomena are significant; thus, the THz region is usually considered as the melting point between electronics and photonics. The multiple application possibilities of THz technology have motivated intense research in THz optoelectronic devices in a quest to close the so-called THz gap.^{1,2} However, drift/diffusion transport in traditional electronic devices sets an upper limit on its frequency of operation; hence, obtaining operation at THz frequencies has proven challenging. This difficulty motivated the exploration of unconventional transport mechanisms such as electron plasma waves in two-dimensional electron gases (2DEGs), whose group velocity is $>10\times$ larger than typical electron drift velocities (i.e., $v_g > 10^8$ cm/s). In general, when THz radiation is radiated upon a 2DEG, it can excite collective oscillations of electrons, the so-called electron plasma waves. The excitation of plasma waves *via* THz irradiation has been observed in Si inversion layers,³ as well as in III-V semiconductors,⁴ and 2D materials.⁵ In particular, 2DEGs in AlGaIn/GaN High Electron Mobility Transistors (HEMTs)

have been the subject of intensive studies.^{6–15} AlGaIn/GaN HEMTs showcase excellent transport properties, evidenced by their high electron mobility >2000 cm²/V s at room temperature.^{16–21}

Efficient coupling of THz radiation into and out of plasma waves is essential for the operation of electron plasma wave-driven devices. Because the wavelength of the electron plasma waves is shorter than that of THz radiation in free space, a coupling structure, such as a periodic grating, is necessary as illustrated in Fig. 1(a). The set of plasma waves supported in these grating-gate structures is given by^{22–24}

$$\omega_p^2 = (n_s e^2 / m^*) * k / \epsilon_o (\epsilon_s + \epsilon_b \coth(kd)), \quad (1)$$

where e is the electron charge, ϵ_s and ϵ_b are the relative permittivities of the layers below and above the 2DEG, respectively, d is the barrier thickness, m^* is the electron effective mass, n_s is the electron concentration, k is the magnitude of the plasma wave vector ($k = 2\pi/P_{UC}$), and P_{UC} is the unit cell period as defined in Fig. 1(a).

In a grating-gate configuration, adjacent unit cells interact with each other, making this a coupled resonant system. In contrast, in a HEMT-array configuration, the periodic addition of ohmic contacts to the 2DEG, i.e., S/D electrodes as depicted in Fig. 1(b), makes adjacent unit cells to become effectively independent. In this configuration, the THz to

^{a)}Email: berardi.sensale@utah.edu

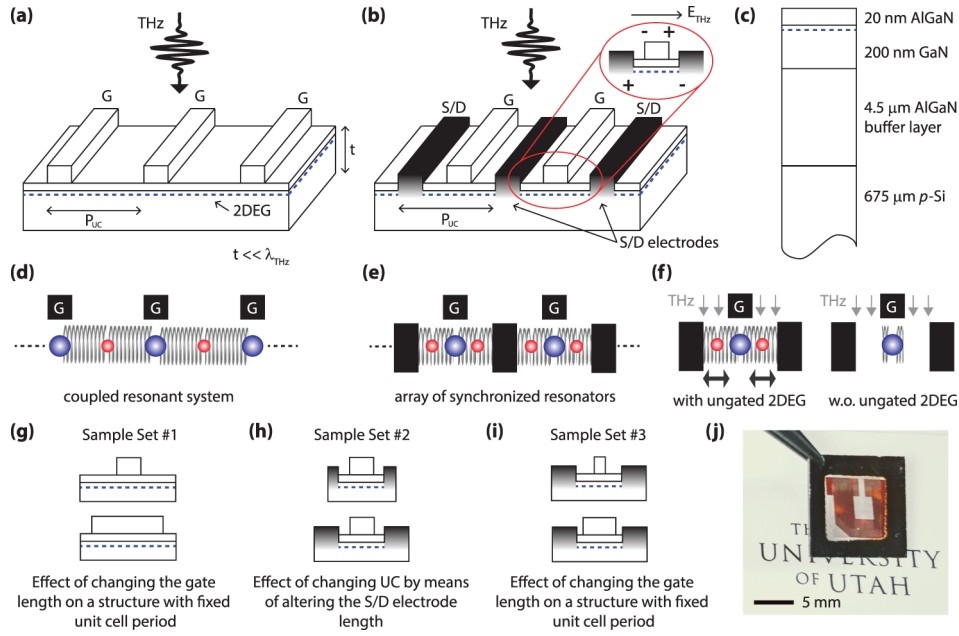


FIG. 1. (a) and (b) Schematic cross-section for the unit cell of: (a) a grating-gate structure and (b) a HEMT-array configuration. The inset shows the oscillating charges of opposite sign across the vertical gap between the gate and ohmic contacts in every unit cell. (c) Layer structure of the employed AlGaIn/GaN HEMT wafer. (d)–(f) Modeling of mobile carrier interactions in the 2DEG via a coupled harmonic resonator. This model allows one to visualize the interaction of charges in each unit cell as well as interaction between adjacent cells; the continuum of charges located below the gate is represented by blue-circles, the continuum of charges located in the ungated 2DEG is represented by red-circles, and the interaction between charges is represented through springs. While in the grating-gate configuration, (d) adjacent unit cells interact with each other, in the HEMT-array configuration and (e) PEC boundary conditions are effectively imposed by the S/D ohmic contacts effectively isolating adjacent unit cells. Furthermore, as depicted in (f), the ungated region has a fundamental role in the coupling of THz radiation. (g)–(i) Illustration of the analyzed sample sets. (j) Optical image of a fabricated sample; the structure is transparent at visible wavelengths owing to its ultra-thin thickness ($\sim 5 \mu\text{m}$).

plasmon coupling can be enhanced by synchronizing the electron plasma waves in each unit cell of the array as theoretically discussed by Popov *et al.*^{25,26}

In this report, we present a systematic experimental demonstration of enhanced THz coupling to electron plasma waves (or plasmons) in ultra-thin membrane HEMT-arrays via plasmon synchronization. A thin-membrane configuration enables us to remove the substrate effects and further enhance the coupling. The proposed approach allows: (i) more efficient excitation of high order plasmonic modes and (ii) superior overall coupling, even in configurations having less number of devices per unit area. Our results reveal a straightforward way to enhance the THz to plasmon coupling and thus improve the performance of electron plasma wave-based devices.

II. ANALYZED SAMPLES

The analyzed samples are schematically depicted in Figs. 1(g)–1(i). In order to provide for a comprehensive study of THz dynamics in these structures, we prepared three sets of samples consisting of: *Sample Set #1: grating-gate HEMT* structures with varied gate lengths (L_G) and a fixed periodicity of the unit cell [Fig. 1(g)]; *Sample Set #2: HEMT-array* structures of varied periodicity of the unit cell with various S/D electrode lengths (L_{SD}), fixed gate lengths, and fixed ungated lengths (L_{UG}) [Fig. 1(h)]; and *Sample Set #3: HEMT-array* structures with a fixed S/D electrode length, fixed periodicity of the unit cell, and varied gate length and ungated length [Fig. 1(i)]. In the context of this

article, we define ungated 2DEG as the region where the 2DEG is not masked by the gate electrode. The dimensions of all the samples under study are summarized in Table I. All samples were fabricated in MOCVD-grown epitaxial structures consisting of a $4.5 \mu\text{m}$ thick AlGaIn-based buffer layer, followed by a 200 nm GaN layer and a 20 nm AlGaIn barrier, which were grown on Si (111). In this structure, a 2DEG is formed at the top AlGaIn/GaN interface. A schematic of the epitaxial structure is depicted in Fig. 1(c). Samples were characterized via Hall-effect measurements; the extracted 2DEG concentration was $7.6 \times 10^{12} \text{cm}^{-2}$ and the extracted mobility was $1620 \text{cm}^2/\text{V s}$. The interface roughness (for a $2 \mu\text{m} \times 2 \mu\text{m}$ area) was $\sim 0.5 \text{nm}$ and the dislocation density was on the order of $\sim 10^9 \text{cm}^{-2}$. Alloyed ohmic contacts (Ti/Al/Ti/Ni/Au) and Schottky gate contacts (Ni/Au) were defined in successive lithography and lift-off steps in a periodic-pattern through direct writing using a Heidelberg PG 101 pattern generator. The center area of the Si substrate was

TABLE I. Gate length, ungated length, S/D length and unit cell period for the analyzed samples.

	Gate length L_G (μm)	Ungated length L_{UG} (μm)	S/D length L_{SD} (μm)	Unit cell period P_{UC} (μm)
S1a	2.3	3.7	...	6
S1b	4.2	1.8	...	6
S2a	2.5	1.8	1.7	6
S2b	2.7	1.8	3	7.5
S2d'	1.8	2.55	1.65	6
S3a	1.0	3.3	1.7	6

etched from the backside by DRIE (Oxford ICP 100). *The resulting samples are ultra-thin HEMT membranes (thickness $\sim 5 \mu\text{m}$) and therefore do not exhibit any substrate-related effects*; an optical image of a representative sample is depicted in Fig. 1(j).

To gain a deeper insight into the coupling mechanisms, it is worth looking at the fundamental differences between the *grating-gate* and *HEMT-array* approaches. In both cases, periodic boundary conditions are set by the periodicity of the structure; however, in the HEMT-array, in addition to these periodic boundary conditions, the S/D contacts effectively impose Perfect Electrical Conductor (PEC) boundary conditions for the plasma waves. As a result, the electrodes physically isolate each unit cell. A further insight into the cell-to-cell interactions in these structures can be obtained by considering the traditional coupled harmonic resonator models shown in Figs. 1(d) and 1(e). The continuum of charges located below the gate and in the ungated region are modeled by circles and the interaction between these is modeled by springs. As shown in Fig. 1(e), PEC boundary conditions imposed by the S/D electrodes effectively isolate adjacent unit cells in the HEMT-array structure, whereas in the case of the grating-gate HEMT configuration [Fig. 1(d)] adjacent unit cells physically interact with each other. As a result, in the HEMT-array approach, the system behaves as an *array of synchronized resonators* whereas in the case of grating-gate approach the system behaves as a *coupled resonant system*.

A common feature that both approaches share is that the ungated region strongly contributes to the coupling of THz radiation into the gated region. When THz radiation impinges upon both structures, it couples into plasmons via the ungated region.²⁷ In the absence of an ungated region, for example, in our experimental case, when the 2DEG in the ungated region is etched away, mobile charges in the gated 2DEG are screened by the metal gate; thus, THz radiation cannot be coupled into plasma waves in the gated region as schematically depicted in Fig. 1(f); as a result, reduction in the coupling of THz radiation to plasma waves is expected.

III. CHARACTERIZATION METHODS

For the purpose of terahertz characterization, a THz time-domain spectroscopy setup (THz-TDS) was employed. In the TDS setup, a broadband THz pulse was generated by optical rectification of an optical pulse in ZnTe crystals. The sample was placed at the focal plane of the THz beam and its response was modulated using electro-optic sampling on a similar ZnTe crystal on the detector side.²⁸ The transmission was Fourier transformed to obtain the spectrum of the signal, which was then normalized to the response of a reference substrate. For measurements at 77 K, the samples were mounted on an optical holder inside a cryostat, which was equipped with a temperature sensor and a heater to control the temperature in the range of 77 K to 400 K.

To compute the THz response of the analyzed samples, Finite Element Method (FEM) simulations were performed using ANSYS HFSS.²⁹ The transmission spectra were numerically calculated with a frequency resolution of 5 GHz. A layer-by-layer model was employed to simulate the

response of the overall structure as discussed in Ref. 27. That is, each layer in the epitaxial hetero-structure was modeled by means of a set of constitutive parameters ϵ , μ , and σ . The THz excitation was defined as a normally incident plane-wave (with respect to the sample) with a polarization perpendicular to the gate fingers. Due to the symmetry of the analyzed structure, just one unit cell was simulated and periodic boundary conditions were set along the x and y directions. The frequency dependent response of the 2DEG at the AlGaIn/GaN interface was described by the following Drude conductivity and permittivity

$$\sigma = \frac{\sigma_0}{1 + \omega^2 \tau^2}; \quad \epsilon = \epsilon_r - \frac{\sigma_0 \tau}{\epsilon_0} \frac{1}{1 + \omega^2 \tau^2}, \quad (2)$$

where, τ is the electron momentum relaxation time, σ_0 is the 2DEG zero-frequency dynamic conductivity, and ϵ_r is the low-frequency relative permittivity of GaN. These parameters were extracted from the fitting of measurements using control samples without metallization.

Transmission line measurements (TLM) were performed on a set of $100 \times 100 \mu\text{m}^2$ ohmic contacts with varied separation, which were placed in the periphery of the samples as depicted in the inset of Fig. 2(a). The results of the electrical measurements are depicted in Fig. 2(a); the extracted contact resistance (R_c) is $1.3 \Omega \text{mm}$ with a 2DEG sheet-conductivity (σ_{DC}) of 1.56 mS (at room temperature). Furthermore, we performed THz TDS measurements through control samples to extract the zero-frequency dynamic conductivity and the momentum relaxation time. These samples consisted of the etched $\sim 5 \mu\text{m}$ thick membrane sample without any metallization. The TDS spectra obtained from these samples were normalized to that through a similar sample without a 2DEG, i.e., a sample where the 2DEG was etched. The TDS results are shown in Fig. 2(b). The structure was modeled employing Ansys HFSS and the experimental results were fitted to the simulations, allowing us to extract the conductivity and the momentum relaxation time for the 2DEG (fitting parameters). The momentum relaxation time that best fits

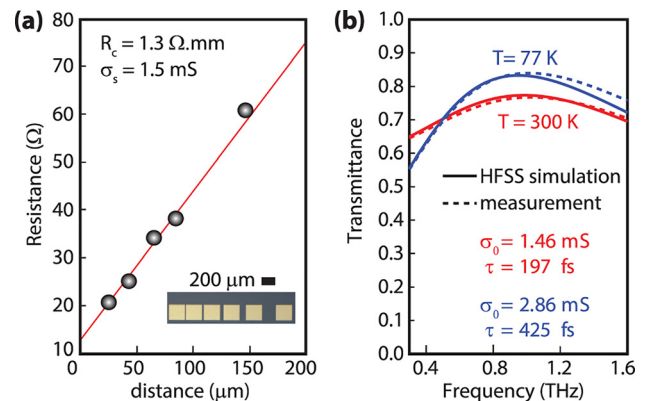


FIG. 2. (a) TLM measurements; a sheet conductivity of $\sim 1.5 \text{ mS}$ was extracted. (b) Measured THz transmission through a control sample; the measured data fits well to numerical simulations (HFSS) employing a Drude model for the 2DEG, the zero-frequency conductivities that best fit the experimental data at 300 K and 77 K are 1.46 and 2.86 mS, respectively; the extracted momentum relaxation times at 300 K and 77 K are 197 and 425 fs, respectively.

the experimental data at 300 K and 77 K is 197 and 425 fs, respectively. These values correspond to 2DEG mobilities of 1732 and 3747 cm^2/Vs . The zero-frequency dynamic conductivities extracted at 300 K and 77 K were 1.46 and 2.86 mS, respectively. These values correspond to 2DEG carrier concentrations of 5.26×10^{12} and $4.78 \times 10^{12} \text{ cm}^{-2}$. The conductivity levels obtained from TDS are in good agreement with those extracted from TLM measurements. These extracted values were employed to numerically model the transmission spectra through the samples.

IV. RESULTS AND DISCUSSION

A. Simulation results

1. The spectral position of the plasmonic resonance shows a stronger gate-length dependence in HEMT-array configurations

To analyze the effect of the gate length on the frequency of resonance, we performed simulations varying the gate-length while keeping the unit cell constant (in both the grating-gate and HEMT-array configurations) as well as the S/D electrode length (in the HEMT-array configuration). In order to reduce the computation time, a semi-infinite substrate was assumed in these simulations. From the numerical simulation results of absorption versus frequency (with absorption defined as $A = 1 - T - R$, where T and R represent transmission and reflection, respectively), contour-plots for the absorption spectra versus gate-length were generated, which are depicted in Figs. 3(a) and 3(b) for the grating-gate and HEMT-array configurations, respectively. The dashed lines represent the spectral position of the frequency of resonance for different resonant modes; these frequencies correspond to local maxima in the absorption spectra. The unit cell was kept constant at $6 \mu\text{m}$ (in both cases). For the HEMT-array structure, the length of the S/D electrodes was set to $1.2 \mu\text{m}$. As observed in Fig. 3(c), for the case of the grating-gate configuration, when decreasing the gate length from 5.9 to $1 \mu\text{m}$, there is a small blue shift in the frequency of resonance. However, for the case of the HEMT-array

configuration, a stronger frequency shift is observed when altering the gate length [Fig. 3(d)]. This supports in part our observations (to be further discussed in following sections): (i) the position of the frequency of resonance in the grating-gate configuration depends mainly on the unit cell period rather than on the gate length and (ii) the position of the frequency of resonance in the HEMT-array configuration depends mainly on the gate length rather than on the unit cell period. Furthermore, Fig. 3 clearly highlights one of the most important advantages of the HEMT-array approach: its ability to more efficiently excite higher order plasmonic resonances.

2. The spectral position of the plasmonic resonance as well as the magnitude of the power absorption shows stronger unit cell period dependences in grating-gate configurations

Further insight into the electromagnetic response of the grating-gate and HEMT-array configurations can be obtained by numerically studying the effect of the unit cell period. Numerical results for the transmission and absorption spectra for grating-gate and HEMT-array configurations are depicted in Figs. 4(a), 4(b), and 4(c), 4(d), respectively. Again, to reduce the computation time, simulations were performed assuming a semi-infinite substrate. In all cases, the gate length was fixed to $2.4 \mu\text{m}$, while the unit cell was varied from $6 \mu\text{m}$ to $15 \mu\text{m}$. For the HEMT-array configuration, the unit cell period was varied by means of changing the S/D electrode length, i.e., $L_{S/D}$ was varied between $0.5 \mu\text{m}$ and $15 \mu\text{m}$, while L_{UG} was fixed to $1.05 \mu\text{m}$. From the transmission spectra for the grating-gate configuration depicted in Fig. 4(a), it is observed that as the unit cell period increases the frequency of resonance shifts towards lower frequencies. Furthermore, from the absorption spectra shown in Fig. 4(b), it is observed that as the unit cell period is increased, the strength as well as the quality factor of the resonance reduce. From this perspective, we found that reducing the separation between adjacent gates is required to enhance the terahertz to plasmon electromagnetic coupling. A similar study was

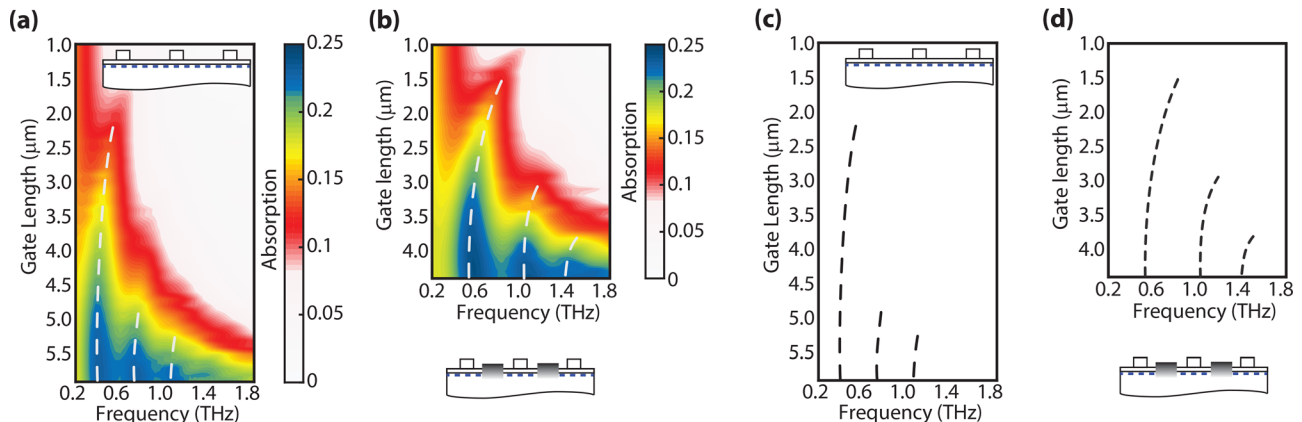


FIG. 3. Simulated THz absorption for (a) a grating-gate configuration and (b) a HEMT-array configuration, for various gate lengths (P_{UC} and $L_{S/D}$ are fixed). The color maps correspond to different absorption levels. The dashed lines map the evolution of the frequency of resonance in both structures when altering the gate-length. Stronger and much well-defined resonance features are observed in the HEMT-array configuration; furthermore, a stronger dependence of the resonance frequency with gate-length is also noticed. These observations agree with our experimental results. (c) and (d) Evolution of the frequency of resonance in the grating gate approach (c) and the HEMT array (d).

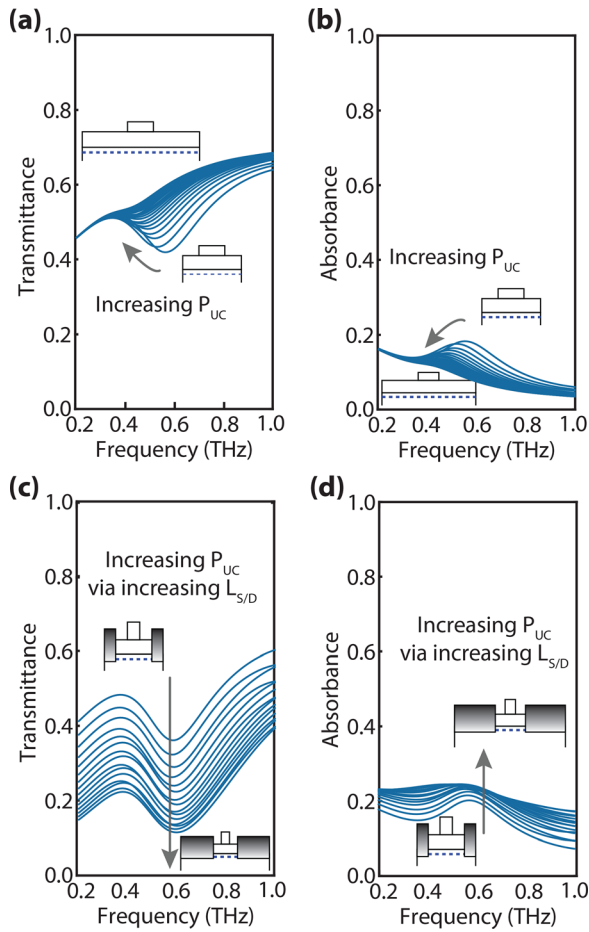


FIG. 4. (a) and (b) Simulated transmission (a) and absorption (b) spectra of a grating-gate configuration when varying the unit cell period. The resonance frequency in this structure has a much stronger dependence on the unit cell period than on L_G ; furthermore, as P_{UC} is increased from $6 \mu\text{m}$ to $15 \mu\text{m}$, smaller absorption is observed. (c) and (d) Simulated transmission (c) and absorption (d) spectra of a HEMT-array configuration when varying the P_{UC} by means of altering $L_{S/D}$.

performed for the HEMT-array configuration, where the results of the simulations for transmission and absorption spectra are shown in Figs. 4(c) and 4(d), respectively. Interestingly, the absorption spectra depicted in Fig. 4(d) indicate that at the frequency of interest the overall absorption levels do not drop when altering the unit cell period in the HEMT-array structure. Furthermore, as also observed in the grating-gate case, the resonance in the HEMT-array structure becomes broader as the unit cell period is increased. From this point of view, absorption cannot longer be considered a resonant process. However, the fact that absorption remains high in these situations can have implications in devices operating in a non-resonant regime (e.g., non-resonant HEMT detectors). From this perspective, our results reveal that by employing a HEMT-array configuration, the number of devices, and thus the total active-area in an array of detectors can be greatly reduced while (i) coupling the same amount of power into the total array and (ii) effectively enhancing the fields in each element of the array,²⁶ but at the expense of (iii) a tradeoff between resonant and non-resonant absorption. Since detection in HEMTs arises from the rectification of THz fields and thus is a

non-linear process, concentrating more power into each element of the array can in principle lead to enhanced responsivity. To illustrate this effect, let us consider the number of devices (N) in an $8 \text{ mm} \times 8 \text{ mm}$ area. For a S/D electrode length of $1.5 \mu\text{m}$, $N = 8000 \mu\text{m} / (2 \times L_{UG} + L_G + L_{S/D}) \sim 1333$ devices. Now, when the S/D electrode length is increased to $15 \mu\text{m}$, the number of devices reduces to $N \sim 410$ devices. While the unit cell is increased by a factor of $(15 + 2.1 + 2.4) / (1.5 + 2.1 + 2.4) \sim 3.25 \times$, the number of HEMTs in the array is effectively reduced by the same factor. It is to be noted that the coupled (absorbed) THz power is identical in both cases; however, the reflected power is increased as the S/D electrode length is increased.

B. Experimental results

1. Unit cells are coupled in grating-gate devices

To study the effect of the gate-length on the frequency of resonance in grating-gate structures, we fabricated samples having a constant periodicity and varied gate-length. For this purpose, we experimentally analyzed the THz transmission through two samples corresponding to *Sample Set #1*, namely: *Samples S1a* and *S1b*. The experimental results for transmission at 77 K are depicted in Figs. 5(a) and 5(b) for *Samples S1a* and *S1b*, respectively. For *Sample S1a*, the first resonance is observed at 0.51 THz, whereas for *Sample S1b*, the first resonance is observed at 0.48 THz. The effect of the gate length on the frequency of resonance in this set of samples is not very strong, although the gate length changed by a factor of ~ 2 , i.e., from 2.3 to $4.2 \mu\text{m}$, the frequency of resonance only decreased from 0.51 to 0.48 THz. Nevertheless, a small frequency shift is observed [see Fig. 5(c)]. Alternatively, if focus is on the separation between gate edges rather than on gate length, it is observed that decreasing the separation between adjacent gates by a factor of 2 while holding the period constant decreases the resonance frequency from 0.51 to 0.48 THz. Furthermore, when

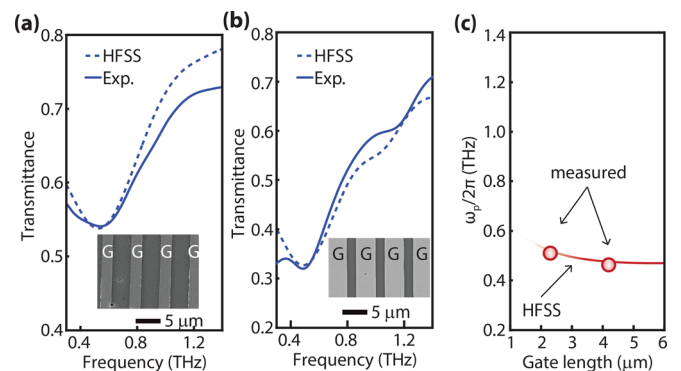


FIG. 5. Simulation and experimental results of *Sample Set #1*. (a) Simulated and measured transmission spectra of *Sample S1a*. The insets depict the SEM detail of the array. (b) Simulated and measured transmission spectra of *Sample S1b*. The insets depict the SEM detail of the array. Measurements were taken at 300 K and 77 K; although weak resonant features were observed at room-temperature (data not shown), which is a result of the short electron momentum relaxation time in GaN at 300 K, well-defined resonances are present at 77 K. (c) Position of the resonance frequency vs. gate-length, a small dependence is observed; furthermore, as the gate-length is reduced, the resonance weakens.

comparing the strength of these resonances, we find that as the separation between adjacent gates is decreased, the resonance is strengthened. In general, reducing the length of the ungated region helps to improve the resonance strength. Our experimental results are in very close agreement with predictions from full-wave electromagnetic simulations as shown in Figs. 5(a) and 5(b). This observation, added to our observations in Sec. IV A, demonstrates that indeed in the grating-gate configuration the unit cell period rather than the gate-length determines the position of the plasmonic resonance.

2. Unit cells are more weakly coupled in HEMT-array devices

To analyze the effect of periodicity on the electromagnetic response of the HEMT-array, we fabricated two samples having similar gate lengths, similar ungated lengths, but different S/D electrode lengths. For this purpose, we measured the transmission spectra of two HEMT-array samples corresponding to *Sample Set #2*, namely: *Samples S2a* and *S2b*. As depicted in Figs. 6(a) and 6(b), both samples exhibit three well-defined resonances at ~ 0.4 , ~ 0.8 , and ~ 1.2 THz, respectively; this is in close agreement with predictions from full-wave electromagnetic simulations shown also in Figs. 6(a) and 6(b). Here, we find that the resonance frequency does not change when the unit cell period is altered by changing the S/D electrode length, while keeping the gate length and the ungated length fixed. Under this configuration, plasmons that exist in adjacent unit cells are effectively isolated by the S/D ohmic contacts. This provides an experimental validation of each unit cell in the HEMT-array being effectively independent. In agreement with our observations and discussion in Sec. IV A, it is observed that as the unit cell increases the frequency of resonance does not shift; this is in sharp contrast with what occurs in the grating-gate

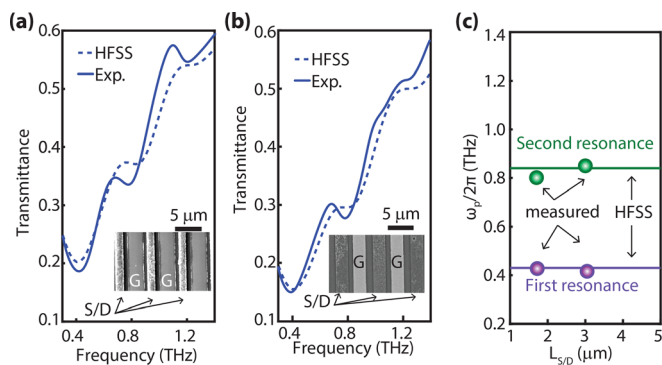


FIG. 6. Simulation and experimental results of *Sample Set #2*. (a) Simulated and measured transmission spectra of *Sample S2a*. The insets depict the SEM detail of the array. (b) Simulated and measured transmission spectra of *Sample S2b*. The insets depict the SEM detail of the array. Both samples, *S2a* and *S2b*, have similar gate-length and ungated length. The unit cell period is varied via changing the length of the S/D electrodes ($L_{S/D}$). Measurements were taken at 300 K and 77 K; although weak resonant features (data not shown) were observed at room-temperature, which is a result of the short electron momentum relaxation time in GaN at 300 K, well-defined resonances are present at 77 K (up to third order). (c) Position of the resonance frequency (first and second resonances) vs. $L_{S/D}$, no dependence is observed.

approach where the *unit cell* defines the position of the frequency of resonance.

3. Decreasing the gate length strongly blue-shifts the resonance in HEMT-array devices

For the purpose of studying the effect of gate-length on the electromagnetic response of the HEMT-array, we fabricated samples with different gate-lengths, same S/D electrode length, and same unit cell period. Thus, an additional HEMT-array sample corresponding to *Sample Set #3: Sample S3b* with a gate length of $1 \mu\text{m}$, was fabricated and measured. This sample is compared to *Sample S2a*, since both samples only differ in the gate length, i.e., both samples have a S/D electrode length of $1.7 \mu\text{m}$ and a unit cell of $6 \mu\text{m}$. The simulated and experimental transmission spectra taken at 77 K are depicted in Fig. 7(a). Whereas for *Sample S2a*, there was a clear resonance at 0.42 THz; in *Sample S3a*, the resonance appears at 0.64 THz. From this perspective, it is observed that the gate length strongly affects the frequency of resonance as shown in Fig. 7(b). Furthermore, a much larger frequency shift is observed when comparing these HEMT-array samples to the grating-gate samples in *Sample Set #1*. Again, the experimental observations are in close agreement with predictions from full-wave electromagnetic simulations by HFSS.

4. Effect of the ungated region on the terahertz to plasmon electromagnetic coupling: There is no coupling if the ungated 2DEG is etched away

Finally, in order to explore the effect and the importance of the ungated 2DEG region in the coupling of terahertz radiation into and out of plasmons in these structures, we etched the ungated region on a HEMT-array sample of geometrical dimensions similar to that in *Sample S2a*. This sample, which we labeled *Sample S2a'*, has $1.8 \mu\text{m}$ gate-length, $1.65 \mu\text{m}$ S/D electrode length, and $6 \mu\text{m}$ unit cell period. To etch the ungated-region, we followed the methods described in Ref. 30 using the electrodes as etching masks. The resulting sample has the 2DEG etched in the ungated regions. The

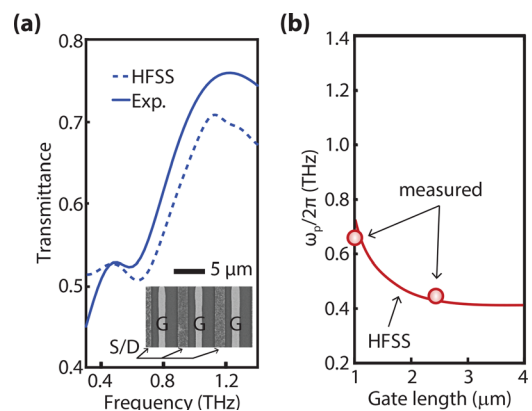


FIG. 7. Simulation and experimental results of *Sample Set #3*. (a) Simulated and measured transmission spectra of *Sample S3a* (a sample having the same unit cell period and same $L_{S/D}$ as *Sample S2a* but with different gate-lengths). The inset depicts a SEM detail of the array. (b) Position of the resonance frequency vs. gate-length, a strong dependence is observed.

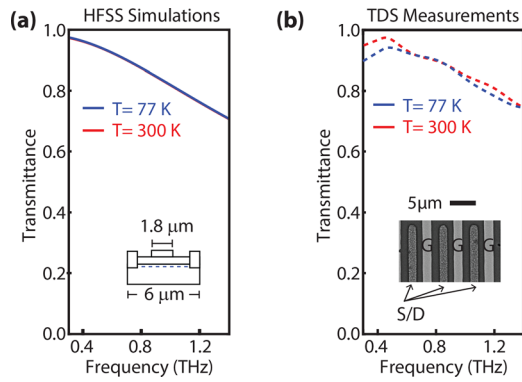


FIG. 8. (a) Simulated transmission spectra of a HEMT-array structure in which the ungated 2DEG was etched away and (b) the corresponding measured transmission spectra. Measurements were taken at 300 K and 77 K; no signatures of plasmonic resonances are observed, which indicate that there is no coupling of THz radiation to plasmons.

measured and simulated transmission spectra are shown in Fig. 8; measurements at 77 K do not show signatures of plasma wave resonance, which confirms the role of the ungated region as an element effectively necessary for the coupling of the incoming terahertz radiation to plasma waves. Again, as in all the discussed examples, our numerical simulation results are in excellent agreement with the experimental data.

V. CONCLUSIONS

In summary, we report on the absorption of terahertz radiation in HEMT-arrays fabricated in AlGaN/GaN thin-membranes. Our experiments and simulations evidence that enhanced coupling of terahertz radiation into plasma waves is possible in this device configuration, which consists of an array of independent synchronized resonators. While in conventional grating-gate devices, only the first and second order resonances were discernible in the transmission spectra, under the same experimental conditions and similar minimum lithographic features, sharper resonant features and higher order resonances (up to the third-order) were observed in HEMT-arrays. By employing the proposed approach, not only the terahertz-to-electromagnetic coupling can be enhanced, especially for higher order modes, but also the number of active devices in the array can be greatly reduced. From these perspectives, our study can pave a way to realizing more efficient and compact plasmonic terahertz devices.

ACKNOWLEDGMENTS

This work was in part supported by the Office of Naval Research MURI, N00014-11-1-0721, monitored by Paul Maki, and by the Air Force Office of Scientific Research (AFOSR), FA9550-17-1-0048, monitored by Ken Goretta. This work was also supported by the NSF MRSEC program

at the University of Utah under Grant No. DMR 1121252 and by the NSF CAREER Award No. 1351389.

- ¹I. F. Akyildiz, J. M. Jornet, and C. Han, *Phys. Commun.* **12**, 16–32 (2014).
- ²M. Tonouchi, *Nat. Photonics* **1**, 97–105 (2007).
- ³S. Allen, D. Tsui, and R. Logan, *Phys. Rev. Lett.* **38**(17), 980–983 (1977).
- ⁴A. V. Muravjov, D. B. Veksler, V. V. Popov, O. V. Polischuk, N. Pala, X. Hu, R. Gaska, H. Saxena, R. E. Peale, and M. S. Shur, *Appl. Phys. Lett.* **96**(4), 042105 (2010).
- ⁵L. Ju, B. Geng, J. Horng, C. Girit, M. Martin, Z. Hao, and F. Wang, *Nat. Nanotechnol.* **6**(10), 630–634 (2011).
- ⁶S. N. Mohammad, A. A. Salvador, and H. Morkoc, *Proc. IEEE* **83**(10), 1306 (1995).
- ⁷Y. Yue, Z. Hu, J. Guo, B. Sensale-Rodriguez, G. Li, R. Wang, F. Faria, T. Fang, B. Song, S. Guo, T. Kosel, G. Snider, P. Fay, D. Jena, and H. Xing, *IEEE Electron Device Lett.* **33**, 988 (2012).
- ⁸D. S. Lee, X. Gao, S. Guo, D. Kopp, P. Fay, and T. Palacios, *IEEE Electron Device Lett.* **32**, 1525 (2011).
- ⁹O. Ambacher, J. Smart, J. R. Shealy, N. G. Weimann, K. Chu, M. Murphy, and M. Stutzmann, *J. Appl. Phys.* **85**(6), 3222–3233 (1999).
- ¹⁰K. S. Im, J. B. Ha, K. W. Kim, J. S. Lee, D. S. Kim, S. H. Hahm, and J. H. Lee, *IEEE Electron Device Lett.* **31**(3), 192–194 (2010).
- ¹¹S. K. O’leary, B. E. Foutz, M. S. Shur, and L. F. Eastman, *J. Mater. Sci.: Mater. Electron.* **17**, 87 (2006).
- ¹²Y. Yue, Z. Hu, J. Guo, B. Sensale-Rodriguez, G. Li, R. Wang, F. Faria, B. Song, X. Gao, S. Guo, T. Kosel, G. Snider, P. Fay, D. Jena, and H. G. Xing, *Jpn. J. Appl. Phys., Part 1* **52**(8S), 08JN14 (2013).
- ¹³E. T. Yu, G. J. Sullivan, P. M. Asbeck, C. D. Wang, D. Qiao, and S. S. Lau, *Appl. Phys. Lett.* **71**(19), 2794–2796 (1997).
- ¹⁴Y. C. Kong, Y. D. Zheng, C. H. Zhou, S. L. Gu, R. Zhang, P. Han, and R. L. Jiang, *Appl. Phys. A: Mater. Sci. Process.* **84**(1), 95–98 (2006).
- ¹⁵S. Rajan and D. Jena, *Semicond. Sci. Technol.* **28**(7), 070301 (2013).
- ¹⁶M. J. Manfra, L. N. Pfeiffer, K. W. West, H. L. Stormer, K. W. Baldwin, J. W. P. Hsu, and R. J. Molnar, *Appl. Phys. Lett.* **77**(18), 2888–2890 (2000).
- ¹⁷S. Keller, G. Parish, P. T. Fini, S. Heikman, C.-H. Chen, N. Zhang, S. P. DenBaars, U. K. Mishra, and Y.-F. Wu, *J. Appl. Phys.* **86**(10), 5850–5857 (1999).
- ¹⁸G. Li, R. Wang, J. Guo, J. Verma, Z. Hu, Y. Yue, F. Faria, Y. Cao, M. Kelly, T. Kosel, H. Xing, and D. Jena, *IEEE Electron Device Lett.* **33**, 661 (2012).
- ¹⁹E. Frayssinet, W. Knap, P. Lorenzini, N. Grandjean, J. Massies, C. Skierbiszewski, T. Suski, I. Grzegory, S. Porowski, G. Simin, and X. Hu, *Appl. Phys. Lett.* **77**(16), 2551–2553 (2000).
- ²⁰A. T. Schremer, J. A. Smart, Y. Wang, O. Ambacher, N. C. MacDonald, and J. R. Shealy, *Appl. Phys. Lett.* **76**(6), 736–738 (2000).
- ²¹J. M. Redwing, M. A. Tischler, J. S. Flynn, S. Elhamri, M. Ahoujja, R. S. Newrock, and W. C. Mitchel, *Appl. Phys. Lett.* **69**, 963–965 (1996).
- ²²A. Eguiluz, T. Lee, J. Quinn, and K. Chiu, *Phys. Rev. B* **11**, 4989 (1975).
- ²³S. Das Sarma and A. Madhukar, *Phys. Rev. B* **23**, 805 (1981).
- ²⁴P. Burke, I. Spielman, J. Eisenstein, L. Pfeiffer, and K. West, *Appl. Phys. Lett.* **76**(6), 745 (2000).
- ²⁵V. Popov, *J. Infrared Millimeter Terahertz Waves* **32**(10), 1178–1191 (2011).
- ²⁶V. Popov, M. Shur, G. Tsymbalov, and D. Fateev, *Phys. Model. Tera-Nano-Devices* **47**, 113–122 (2008).
- ²⁷H. O. Condori Quispe, J. J. Encomendero-Risco, H. G. Xing, and B. Sensale-Rodriguez, *Appl. Phys. Lett.* **109**(6), 063111 (2016).
- ²⁸A. Nahata, A. S. Weling, and T. F. Heinz, *Appl. Phys. Lett.* **69**, 2321 (1996).
- ²⁹ANSYS HFSS, <http://www.ansoft.com/products/hf/hfss/> for “3D Full-wave Electromagnetic Field Simulation by Ansoft.”
- ³⁰T. Sreenidhi, K. Baskar, A. DasGupta, and N. DasGupta, *Semicond. Sci. Technol.* **23**(12), 125019 (2008).